

Machine learning reveals systematic accumulation of electric current in lead-up to solar flares

Author(s): Dattaraj B. Dhuri, Shravan M. Hanasoge and Mark C. M. Cheung

Source: *Proceedings of the National Academy of Sciences of the United States of America*, June 4, 2019, Vol. 116, No. 23 (June 4, 2019), pp. 11141-11146

Published by: National Academy of Sciences

Stable URL: <https://www.jstor.org/stable/10.2307/26706421>

JSTOR is a not-for-profit service that helps scholars, researchers, and students discover, use, and build upon a wide range of content in a trusted digital archive. We use information technology and tools to increase productivity and facilitate new forms of scholarship. For more information about JSTOR, please contact support@jstor.org.

Your use of the JSTOR archive indicates your acceptance of the Terms & Conditions of Use, available at <https://about.jstor.org/terms>



JSTOR

National Academy of Sciences is collaborating with JSTOR to digitize, preserve and extend access to *Proceedings of the National Academy of Sciences of the United States of America*

Machine learning reveals systematic accumulation of electric current in lead-up to solar flares

Dattaraj B. Dhuri^{a,1}, Shravan M. Hanasoge^{a,b}, and Mark C. M. Cheung^{c,d}

^aDepartment of Astronomy and Astrophysics, Tata Institute of Fundamental Research, Mumbai 400005, India; ^bCenter for Space Science, New York University Abu Dhabi, Abu Dhabi, United Arab Emirates; ^cLockheed Martin Solar & Astrophysics Laboratory, Lockheed Martin Advanced Technology Center, Palo Alto, CA 94304; and ^dHansen Experimental Physics Laboratory, Stanford University, Stanford, CA 94305

Edited by Katepalli R. Sreenivasan, New York University, New York, NY, and approved April 17, 2019 (received for review November 29, 2018)

Solar flares—bursts of high-energy radiation responsible for severe space weather effects—are a consequence of the occasional destabilization of magnetic fields rooted in active regions (ARs). The complexity of AR evolution is a barrier to a comprehensive understanding of flaring processes and accurate prediction. Although machine learning (ML) has been used to improve flare predictions, the potential for revealing precursors and associated physics has been underexploited. Here, we train ML algorithms to classify between vector-magnetic-field observations from flaring ARs, producing at least one M-/X-class flare, and nonflaring ARs. Analysis of magnetic-field observations accurately classified by the machine presents statistical evidence for (i) ARs persisting in flare-productive states—characterized by AR area—for days, before and after M- and X-class flare events; (ii) systematic preflare buildup of free energy in the form of electric currents, suggesting that the associated subsurface magnetic field is twisted; and (iii) intensification of Maxwell stresses in the corona above newly emerging ARs, days before first flares. These results provide insights into flare physics and improving flare forecasting.

solar flares | space weather | solar magnetic fields | machine learning

By virtue of buoyancy, magnetic fields generated in the interior of the Sun rise to the photosphere—the visible solar surface—and emerge as bipolar active regions (ARs) (1, 2). Emerging flux and electric currents energize the coronal magnetic field that is rooted in ARs (3). Magnetic reconnection occasionally releases free energy built up in the coronal loops in violent events such as solar flares (4, 5). M- and X-class flares, producing X-ray flux $>10^{-5}$ W·m⁻² and $>10^{-4}$ W·m⁻², respectively, as measured by the Geostationary and Environmental Satellite (GOES), can have severe space weather consequences (6). Operational flare forecasts are based on subjective analyses of AR morphology (7–9). Reliable precursors for accurate flare forecasting, however, remain elusive (10).

The complex nature of AR dynamics hinders straightforward interpretation of flare observations, although AR magnetic-field features related to flare activity are known from case and statistical studies (11–13). Recurrent flares are found to be associated with continuously emerging magnetic flux (14). ARs producing M- and X-class flares contain a prominent high-gradient region separating opposite polarities (15). Magnetic helicity and electric current are found to be accumulated in ARs before major flares (16, 17). Minutes before the onset of flares, increased Lorentz forces in ARs are observed as a result of elevated pressure from the coronal magnetic field (18, 19). Such AR features can be quantified using photospheric vector-magnetic-field data (20) from the Helioseismic and Magnetic Imager (HMI) (21) on board the Solar Dynamics Observatory (SDO) (22).

Machine learning (ML)—efficient in classifying, recognizing, and interpreting patterns in high-dimensional datasets—has been applied to predict flares using many AR features simultaneously. Such studies are aimed at developing a reliable forecasting method and identifying features most relevant to

flare activity (23–26), obtaining new AR features that yield better forecasting accuracy (25, 27), and comparing performances of different ML algorithms (28). Flare prediction accuracy is expected to depend on forward-looking time, i.e., how far in advance flares can be predicted. Existing studies, which use AR observations ranging from 1 h to 48 h before flares, suggest, however, that forecasting accuracy is largely insensitive to forward-looking time (24, 27, 29). Thus, flaring ARs may exist in a flare-productive state long before producing a flare. This motivates the present work where we explicitly train ML algorithms to classify between photospheric magnetic fields of flaring and nonflaring ARs. The trained machine builds a correlation (probability distribution function) between AR photospheric magnetic fields and flaring activity in AR coronal loops. We analyze time evolution of machine correlation between AR magnetic fields and flaring activity to investigate (i) whether magnetic fields from flaring and nonflaring ARs are intrinsically different, (ii) statistical evolution in flaring ARs days before and after flares, and (iii) the development of emerging ARs days before first flares.

Methods

We consider ARs between May 2010 and April 2016. Using the GOES X-ray flux catalog (30), we identify ARs that produce at least one M- or X-class flare during its passage across the visible solar disk as flaring and otherwise as nonflaring. We consider only ARs with maximum observed area >25 Mm². This restriction serves to eliminate thousands of very small-scale nonflaring ARs and no flaring AR. We represent AR photospheric magnetic fields by 12 features, listed in Table 1, computed from HMI magnetograms every

Significance

Reliable flare forecasting is essential for improving preparedness for severe space weather consequences. Flares also serve as probes of solar magnetic processes and the emergence of flux at the solar surface. Training machine-learning (ML) algorithms using magnetic-field observations for improving flare forecasting has been extensively studied in prior literature. Instead, here we use ML to understand the underlying mechanisms governing flares. We train ML algorithms to classify flaring and nonflaring active regions (ARs) with high fidelity and report statistical trends for AR evolution days before and after M- and X-class flares. These trends are interpreted in terms of existing models of subsurface magnetic field and flux emergence. Our results also provide hypotheses for achieving reliable flare forecasting.

Author contributions: S.M.H. and M.C.M.C. designed research; D.B.D. performed research; D.B.D. analyzed data; and D.B.D., S.M.H., and M.C.M.C. wrote the paper.

The authors declare no conflict of interest.

This article is a PNAS Direct Submission.

Published under the PNAS license.

¹To whom correspondence should be addressed. Email: dattaraj.dhuri@tifr.res.in.

This article contains supporting information online at www.pnas.org/lookup/suppl/doi:10.1073/pnas.1820244116/-DCSupplemental.

Published online May 20, 2019.

Table 1. Data used for classification of flaring and nonflaring ARs: AR magnetic-field features (SHARPs) used for training ML algorithms

	Symbol	Description
1	USFLUX	Total unsigned flux
2	AREA	Area of strong-field pixels in active region
3	TOTUSJH	Total unsigned current helicity
4	TOTPOT	Total photospheric magnetic free-energy density
5	TOTUSJZ	Total unsigned vertical current
6	TOTBSQ	Total magnitude of Lorentz force
7	ABSNJZH	Absolute value of net current helicity
8	SAVNCP	Sum of modulus of net current of each polarity
9	MEANPOT	Mean photospheric magnetic free energy
10	SHRGT45	Fraction of area with magnetic field shear $>45^\circ$
11	R.VALUE	Sum of flux near polarity inversion line (PIL)
12	TOTFZ	Sum of z component of Lorentz force

These features are correlated with flare activity, yielding optimum flare-forecasting accuracy (24, 31).

12 min (SI Appendix, Table S1). These features are publicly available in the data-product Space Weather HMI Active Region Patches (SHARPs) (31, 32) and produce optimum flare-forecasting performance (24). Using ML, we classify whether a given magnetic-field observation, represented by SHARP features, corresponds to a flaring or nonflaring AR. Part of the available data is used to train the machine and validate the performance. The trained machine is then used to classify and analyze magnetic fields of ARs in the remaining unseen data—the test data. Formally, the trained machine gives an optimum mapping $\mathbf{X} \rightarrow Y$ where \mathbf{X} is a 12-dimensional SHARP feature vector and $Y \in \{1, 0\}$ is the machine prediction. $Y = 1$ implies that the AR has flared or is about to, and $Y = 0$ implies that the AR belongs to the nonflaring population. For flaring ARs, SHARP feature vectors that yield $Y = 1$ are true positives (TPs) and $Y = 0$ are false negatives (FNs). For nonflaring ARs, SHARP feature vectors that yield $Y = 0$ are true negatives (TNs) and $Y = 1$ are false positives (FPs). We statistically analyze time series of SHARP feature vectors $\mathbf{X}(t)$ from TP and FN populations days before and after flares.

Results

Classification of Flaring and Nonflaring Active Regions. We chronologically split the available AR data into two parts. The training and validation data comprise ARs between May 2010 and December 2013 and the test data comprise ARs between January 2014 and April 2016. We explicitly study the development of newly emerged ARs, identified from the first recorded observation within $\pm 60^\circ$ of the central meridian. Between May 2010 and April 2016, only 22 flaring ARs emerged on the visible solar disk, and hence all “emerging ARs” are included in the test data. The total number of ARs considered is listed in Table 2.

We consider observations from flaring ARs which are within ± 72 h of M- or X-class flares for training. Note that all magnetic-

Table 2. Data used for classification of flaring and nonflaring ARs: Number of ARs and M- and X-class flares considered

Row	Training data		Test data	
	I	II	III	
No. flaring ARs	85	66	22	
No. nonflaring ARs	308	273	190	
No. M-class flares	304	276	57	
No. X-class flares	24	12	1	

Nomenclature: I, May 2010–December 2013 (excluding emerging ARs); II, January 2014–April 2016 (excluding emerging ARs); III, May 2010–April 2016 emerging ARs. Machines are trained using SHARP features from ARs in training and validation data with 10-fold cross-validation. Predictions are made on ARs in the test data. Emerging ARs are defined as newly appearing within $\pm 60^\circ$ of the central meridian.

field observations from ARs in the training and validation data are not needed to optimally train the machines. Instead, we pick an observation every 96 min from within ± 6 h of flares and every 864 min otherwise (within ± 72 h of flares). For nonflaring ARs, we pick an observation every 900 min for training. The choice of these time intervals is inconsequential to the results as long as the number of AR observation samples is adequate for training. For robust training, we apply 10-fold cross-validation. We randomly split the flaring and nonflaring ARs in the training and validation data in 10 parts and use observations from ARs in 9 parts for training and the remaining part for validation. This process is repeated 10 times. Thus, we avoid mixing AR observations in the training and validation sets and thereby avoid artificially boosting the machine performance (28). Total numbers of observations used for training from flaring ARs and nonflaring ARs are 768 and 4,323, respectively (SI Appendix, Table S2).

A straightforward performance measure for classification problems is accuracy, defined as the fraction of correctly classified observations; i.e., $\text{accuracy} = (\text{TP} + \text{TN}) / (\text{TP} + \text{FN} + \text{FP} + \text{TN})$. However, there are five times as many nonflaring as flaring ARs in the training and validation data. Hence, the classification problem considered here is class imbalanced and accuracy is not useful (24). *Recall*, defined as the accuracy for each class, is a more relevant performance metric. For the positive class, i.e., flaring ARs, $\text{recall} = \text{TP} / (\text{TP} + \text{FN})$. Using the training and validation dataset, we compare performance of three ML algorithms—logistic regression (Logit), support vector machines (SVM), and gradient boosting (GB)—for classification of flaring and nonflaring ARs (SI Appendix). SVM yields slightly higher 10-fold cross-validation *recall* value 0.83 ± 0.12 (SI Appendix).

Time Evolution of Machine Prediction. We are particularly interested in time evolution of magnetic fields in flaring ARs, and hence we obtain *recall* of the machine prediction on time series of observations from flaring ARs. A time series $\mathbf{X}(t)$ of SHARP feature vectors representing continuous AR observations yields a time series of machine prediction $Y(t)$. Flares are known to be temporally clustered (33) and hence we focus on evolution within ± 72 h of flares. We compile time series of observations during a window $t - T_F \in [-72, 72]$ h centered around a

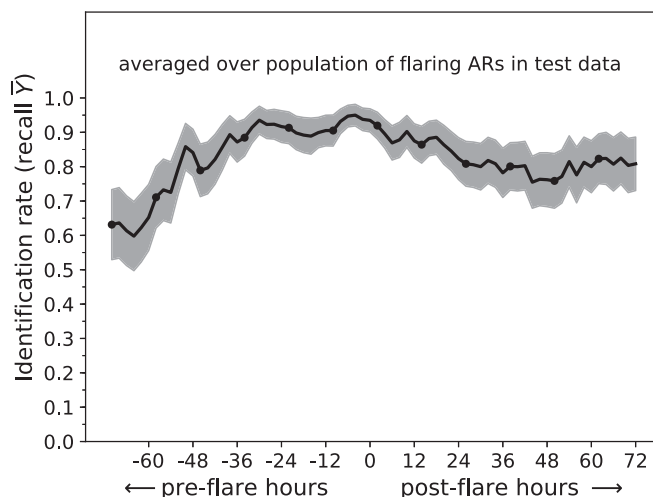


Fig. 1. Time evolution of $\text{recall } \bar{Y}(t) = 1/N(t) \sum_{i=1}^{N(t)} Y_i(t)$ for flaring ARs in the test data before and after a flare using SVM. The *recall* peaks at ~ 0.9 , 24 h before flares. For comparison, machine identification error rate (false-positive rate) for nonflaring ARs in the test data (\bar{Y}) is ~ 0.1 (Table 3). Shaded area indicates 1σ error bar.

Table 3. Average prediction and classification for all flaring and nonflaring AR observations in the test data using SVM

Row	Flaring ARs		Nonflaring ARs
	>72 h from flare event	24 h before flare event	
No. observations	7,952	34	43,055
Recall	0.750 ± 0.085	0.913 ± 0.046	0.889 ± 0.027

Recall value is high even for flaring AR observations, separated from flare events by more than 72 h, and nonflaring AR observations. For flaring AR observations 24 h before flares, machine prediction yields recall of 0.91 which is comparable with reported results (24).

flare event T_F . Whenever two consecutive flares on an AR are separated by <144 h, we split the observations between the flare events into two halves and consider the first half as the postflare category of the first flare and the second half as belonging to the preflare category of the second flare. We align all such time series from flaring ARs at $t - T_F = t_r = 0$, the time of flare events, yielding cotemporal $\mathbf{X}(t_r)$ and $Y(t_r)$ time series for time t_r with respect to the flare. The machine prediction averaged over the flaring-AR population $\bar{Y}(t_r) = (1/N(t_r)) \sum_{i=1}^{N(t_r)} Y_i(t_r)$ gives instantaneous recall or identification rate at time t_r . Here, $N(t_r)$ is the number of magnetic-field observations available at time t_r from the flaring-AR population (SI Appendix, Fig. S2). Thus, recall $\bar{Y}(t_r)$ is a measure of the time-evolving correlation between SHARP features and flare activity, obtained using the trained machine. Similarly, the machine predictions can be obtained for all observations from nonflaring ARs. Since there is no characteristic time event on nonflaring ARs, we find the average machine prediction defined as $\langle Y \rangle = (1/N) \sum_i Y_i$. $\langle Y \rangle$ is time and population average over all N nonflaring AR observations and gives the false-positive rate.

We can now obtain time evolution of machine prediction for flaring ARs in the test data using the trained SVM. Note that none of the observations from the test data were considered during training and cross-validation of the machine, i.e., SVM, performance. Thus, all observations in the test data are previously “unseen” by the machine. Similar to the training data, recall or identification rate is consistently high (>0.6) for days before and after flares for flaring ARs in the test data (Fig. 1). This indicates that flaring ARs persist in a flare-productive state for days before and after flares. With proximity to flares, identi-

cation rate increases to a maximum of 0.91, 24 h before flare. This recall value is comparable to reported results of flare forecasting using ML (24) and significantly higher than recall ~ 0.55 obtained through operational forecasts based on subjective AR analyses (as estimated by ref. 9).

The number of observations separated from flares by >72 h reduces significantly to continue time evolution analysis beyond 72 h before and after flares (SI Appendix, Fig. S2). Hence, we obtain time- and population-averaged machine prediction $\langle Y \rangle_{\text{flaring}} = (1/N_{\text{flaring}}) \sum_i^{N_{\text{flaring}}} Y_i$, where N_{flaring} is the number of all flaring AR observations separated from flares >72 h. $\langle Y \rangle_{\text{flaring}}$ thus gives recall for such flaring AR observations. Similarly, recall for nonflaring ARs is obtained by $1 - \langle Y \rangle_{\text{nonflaring}}$. Time- and population-averaged values of recall for flaring and nonflaring ARs are reported in Table 3. The high value of recall ~ 0.75 even for observations separated from flares >72 h suggests that SHARP features derived from magnetic fields of flaring ARs are statistically significantly different from those of nonflaring ARs.

Evolution of Magnetic Fields in Flaring Active Regions. We have trained an SVM to distinguish between SHARP features derived from magnetic fields in flaring and nonflaring ARs with high fidelity. To understand magnetic-field evolution in ARs, we analyze TP and FN populations from flaring ARs and TN and FP populations from nonflaring ARs, as categorized by the machine. We include SHARP features from all ARs in the training and validation data as well as the test data. In Table 4, time- and population-averaged values of SHARP features over flaring AR observations separated from flares >72 h and nonflaring AR observations are listed. As expected, average TP (also FP) values are strikingly higher than average TN (also FN) values. This difference is listed in terms of SD of average TN values for each of the SHARP parameters, in the last column in Table 4. Total unsigned flux (USFLUX) and total unsigned current helicity (TOTUSJH) are leading contributors to machine classification. Whereas mean free energy (MEANPOT) and area with shear >45° (SHRGT45) minimally influence the classification. Also, SHARP features that lead classification between flaring and nonflaring ARs are an extensive measure of AR magnetic field.

Categories of SHARP features are further highlighted by the Pearson correlation matrix in Fig. 2. Strongly correlated features are divided into the following groups: (i) extensive features (area, total unsigned flux, total free energy, total Lorentz force, total

Table 4. Average values of SHARP features over flaring and nonflaring AR magnetic-field observations categorized by the SVM

Symbol	Brief description	Flaring ARs, >72 h from flare		Nonflaring ARs		(TP – TN)/ σ_{TN}
		TP	FN	FP	TN	
USFLUX, 10^{22} Mx	Total unsigned flux	3.30 ± 0.29	1.07 ± 0.11	2.48 ± 0.19	0.56 ± 0.03	94.71
TOTUSJH, 10^2 G ² /m	Total unsigned current helicity	23.87 ± 2.09	7.89 ± 0.81	19.45 ± 1.42	4.29 ± 0.21	91.27
TOTBSQ, 10^{10} G ²	Total Lorentz force	4.43 ± 0.41	1.53 ± 0.17	3.57 ± 0.32	0.83 ± 0.04	89.10
TOTUSJZ, 10^{13} A	Total unsigned vertical current	5.43 ± 0.45	1.86 ± 0.21	4.48 ± 0.35	1.00 ± 0.05	85.68
TOTFZ, 10^{23} dyne	Total vertical Lorentz force	–3.30 ± 0.51	–0.61 ± 0.19	–1.55 ± 0.20	–0.34 ± 0.04	78.54
SAVNCPP, 10^{13} A	Sum of net current per polarity	1.14 ± 0.11	0.39 ± 0.05	0.93 ± 0.10	0.24 ± 0.01	74.70
ABSJNZH, G ² /m	Absolute net current helicity	254.59 ± 31.95	68.37 ± 12.66	208.28 ± 28.53	40.68 ± 2.92	73.23
TOTPOT, 10^{23} erg/cm	Total magnetic free energy	5.20 ± 0.61	1.44 ± 0.30	4.80 ± 0.61	0.72 ± 0.06	71.71
AREA, Mm ²	AR area	262.17 ± 19.99	110.95 ± 11.88	222.82 ± 18.35	62.75 ± 2.81	71.00
R.VALUE, Mx	Flux near polarity inversion line	4.06 ± 0.09	2.81 ± 0.25	4.04 ± 0.08	2.09 ± 0.09	20.95
SHRGT45, %	Area with shear >45°	29.76 ± 1.85	24.87 ± 3.81	37.30 ± 2.04	20.24 ± 1.17	8.10
MEANPOT, 10^2 erg/cm ³	Mean magnetic free energy	68.34 ± 4.61	54.82 ± 10.08	81.42 ± 6.64	45.51 ± 3.04	7.51

True positives (TP) and false negatives (FN) are observations from flaring ARs which are classified as flaring and nonflaring, respectively. True negatives (TN) and false positives (FP) are observations from nonflaring ARs that are classified as nonflaring and flaring, respectively.

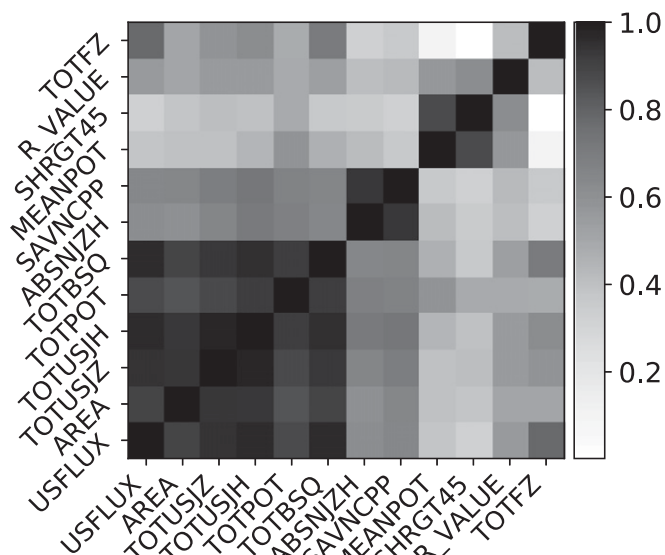


Fig. 2. Pearson correlation matrix for SHARP features (see Table 1 for description). Based on the degree of correlation, SHARP features group together in categories representing (i) AR magnetic-field scale, (ii) AR energy buildup, (iii) AR nonpotentiality, (iv) Schrijver R value, and (v) Lorentz force on AR. P value of correlation between total vertical Lorentz force (TOTFZ) and R value is 0.09. All other P values are $\ll 0.001$.

unsigned vertical current, and total unsigned current helicity), (ii) features that scale with electric current in AR (absolute net current helicity and sum of net current per polarity), (iii) measures of AR nonpotential energy (mean free energy and area with shear $>45^\circ$), (iv) sum of flux near polarity inversion line (15), and (v) vertical Lorentz force on AR. From Table 4, we see that the extensive features dominate machine classification, fol-

lowed by the features that scale with electric current. Meanwhile, features that scale with AR mean nonpotential energy contribute the least.

SHARP features from each of the groups above characteristically evolve before and after flares. For the m th entry of each SHARP feature vector, we calculate the time evolution of population-averaged value $\bar{X}^m(t_r)$, before and after flares, over TP and FN flaring AR observations. SHARP features that scale with AR size are significantly correlated with flare activity. However, similar to total unsigned magnetic flux (Fig. 3A) and total unsigned current helicity (Fig. 3B), average TP values of these SHARP features remain approximately constant before and after flaring and thus characterize flaring AR populations. The average TP value of absolute net current helicity (and also the sum of net current per polarity) systematically increases by about two times during the lead-up to the flare and decreases subsequently (Fig. 3C). This implies that free-energy buildup in large-scale ARs, manifested in field measurements in the form of photospheric electric current, is dominantly responsible for flares (4, 17). The high, distinct average-TP value of flux in the neighborhood of the magnetic polarity inversion line (Fig. 3D) is also a striking feature of flaring ARs (15). AR-associated nonpotential energy, which is weakly correlated with electric current (Fig. 2), is not a leading criterion to discriminate between flaring and nonflaring ARs (Fig. 3E). However, the average FN value of nonpotential energy shows a sharp increase hours before flare. The average TP value of total vertical Lorentz force (Fig. 3F) also systematically decreases from days before flares.

Development of Emerging Flaring ARs. Our analysis shows that extensive SHARP features characteristically distinguish flaring and nonflaring AR populations. Also, values of the extensive features remain approximately constant days before and after flares. On the contrary, newly emerged ARs must start with small values of the extensive SHARP features. Therefore, we are interested in

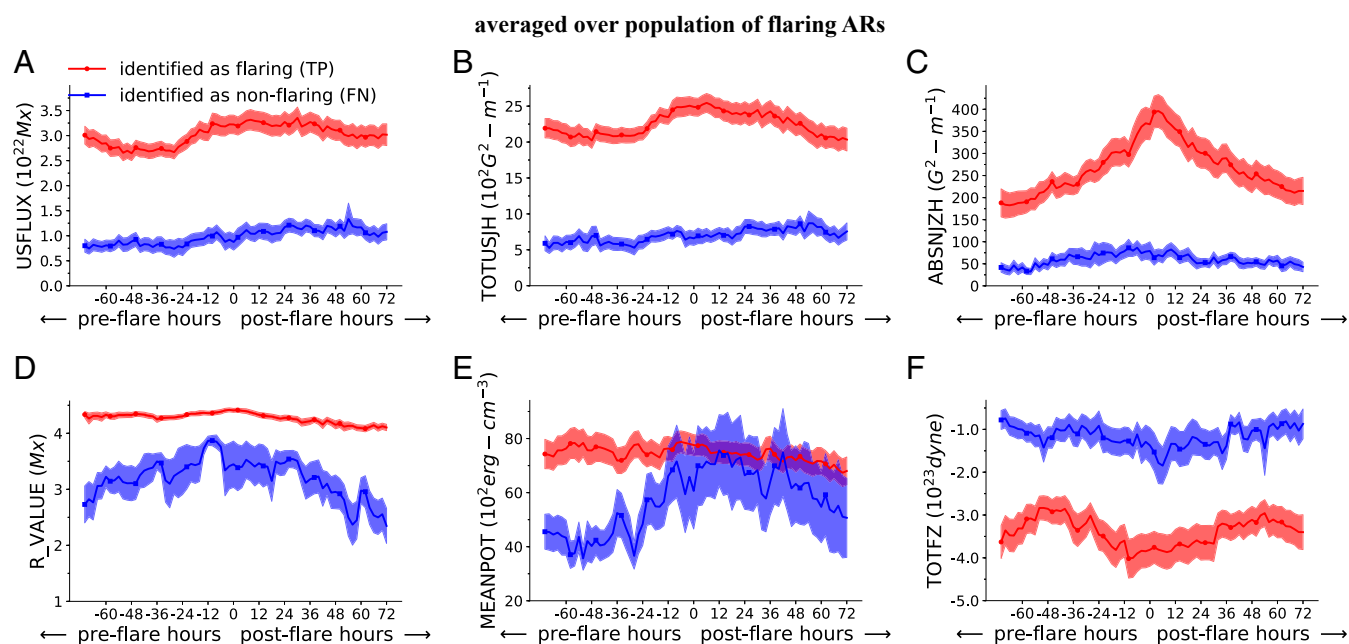


Fig. 3. Time evolution of population-averaged values of SHARP features (see Table 1 for description) before and after flares. Average SHARP feature values over true positive (TP) and false negative (FN) flaring AR observations within ± 72 h of flare events are obtained. Average TP value of total unsigned flux (A) and total unsigned current helicity (B) remains approximately constant before and after flares. Average TP value of absolute net current helicity (C) shows a characteristic steady preflare increase and decrease postflare. Sum of flux near polarity inversion line (R value) (D) also shows a distinct average TP value. For AR nonpotential energy (E), average FN value undergoes a sharp increase ~ 12 h before flares. Average TP value of vertical Lorentz force (F) shows continuous preflare decrease, i.e., increase in downward-directed Lorentz force on the AR. Shaded area indicates 1σ error bars. Key in A applies to A–F.

averaged over population of emerging flaring ARs

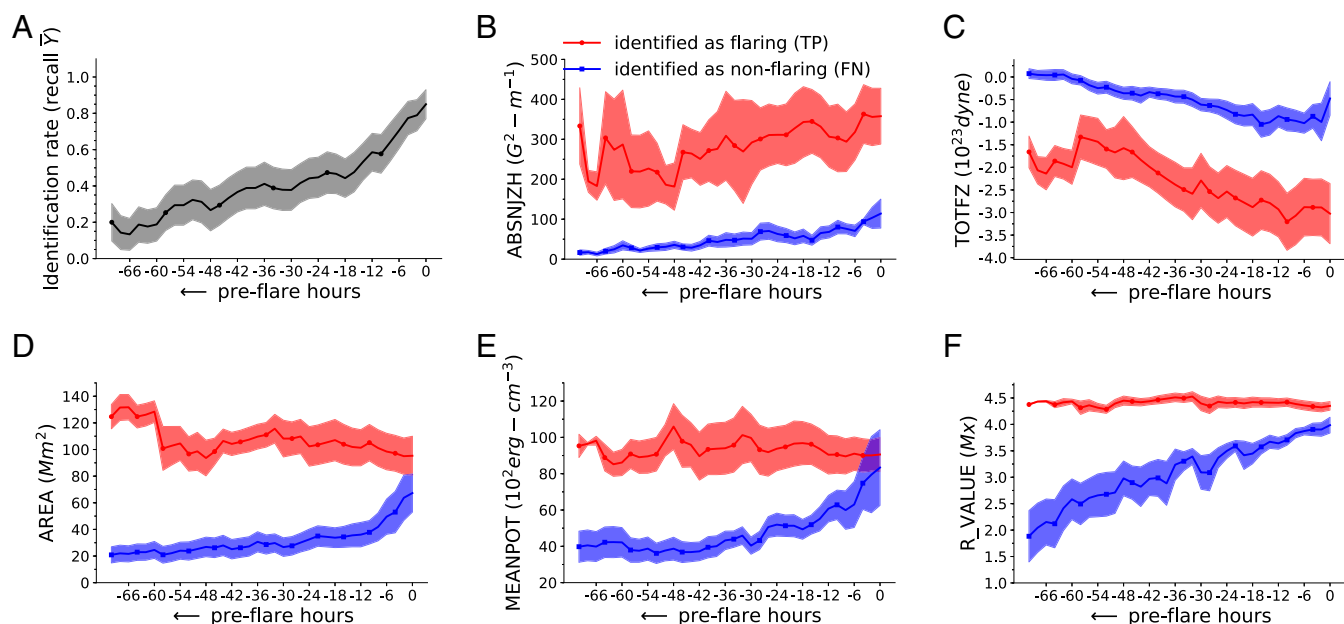


Fig. 4. Machine identification and time evolution of SHARP features for emerging flaring ARs. These emerging ARs are first observed within $\pm 60^\circ$ of the central meridian. (A) Evolution of population-averaged identification rate or *recall* $\bar{Y}(t_r) = 1/N(t_r) \sum_i Y_i(t_r)$ over emerging flaring ARs before 72 h of first flare is shown. For comparison, machine identification error rate (false-positive rate) (\bar{Y}) for emerging nonflaring ARs is ~ 0.1 . (B–F) Time evolution of population-averaged values of SHARP features (see Table 1 for description) over true positive (TP) and false negative (FN) emerging flaring AR observations 72 h before first flare. (B) Average TP value of absolute net current helicity increases steadily before flares. (C) Average TP value of vertical Lorentz force on ARs systematically decreases before flares, i.e., increase in downward-directed Lorentz force. (D and E) Average FN values of area (D) and nonpotential energy (E) increase sharply hours before flares. (F) Average FN value of R value increases gradually before flares. Shaded area indicates 1σ error bars. Key in B applies to B–F.

understanding how emerging ARs transition to flare-productive states before the first flare. For emerging flaring ARs, we compile observations in a time span $t_r \in [-72, 0]$ h where $t_r = t - T_F$ is time with respect to the first-flare event T_F and compute *recall* $\bar{Y}(t_r)$ and TP and FN population-average values for each m th SHARP feature $\bar{X}^m(t_r)$. We see that the machine identification or *recall* of newly emerged ARs steadily improves with time and yields a maximum *recall* value of ~ 0.7 , 6 h before the first flares (Fig. 4A). In comparison, the false-positive rate for emerging nonflaring ARs is ~ 0.1 (*recall* ~ 0.9). For emerging flaring ARs, the population-averaged TP value of absolute net-current helicity (Fig. 4B) shows a steady increase, albeit the error bars are significant. Most notably, the population-averaged TP value of vertically downward-directed Lorentz force increases continuously from days before the flare (Fig. 4C). This may be interpreted as evidence of Maxwell-stress buildup in the corona above flaring active regions, which imparts an enhanced downward-directed Lorentz force on the photosphere. For FNs in the emerging flaring AR observations, area (Fig. 4D) and mean nonpotential energy (Fig. 4E) show marked increase hours before flare.

Discussion

We have trained an SVM to classify SHARP features derived from magnetic fields of flaring and nonflaring ARs. The SHARP features used for training (Table 1) include extensive AR magnetic-field features, features that scale with electric current in ARs representing energy buildup, features that scale with AR nonpotential energy, flux near the polarity inversion line, and vertical Lorentz force on ARs. The trained machine classifies flaring AR observations, separated from flare events >72 h, with an average *recall* of 0.75 and nonflaring AR observations with an average *recall* of 0.89. We compare

time- and population-averaged values of TP (FN) observations from flaring ARs, separated from flares >72 h, and TN (FP) observations from nonflaring ARs. We find that extensive AR quantities are leading contributors to the machine classification followed by AR features that scale with electric current. Features derived from AR nonpotential energy contribute the least.

A time series of AR magnetic-field observations in the form of SHARP features $\mathbf{X}(t)$ when fed into the trained SVM results in machine prediction $\bar{Y}(t)$. Average machine prediction at instant t_r , with respect to flares, over a population of flaring ARs gives instantaneous *recall* $\bar{Y}(t_r)$. $\bar{Y}(t_r)$ can be interpreted as time-evolving correlation of SHARP features with flare activity. We find that instantaneous *recall* is consistently high, >0.6 , for flaring AR observations from 72 h prior, increasing to a maximum of 0.91, 24 h before the flare. The *recall* remains high postflare, suggesting that the ARs lie in a flare-productive state days before and after flares.

Since the machine prediction $\bar{Y}(t_r)$ is a measure of correlation between SHARP features and flare activity, the temporal evolution of features from accurately classified flaring AR observations, i.e., the TP population, reveals precursors to M- and X-class flares. Similarly, the statistical evolution of inaccurately classified flaring AR observations, i.e., the FN population, has trends that the machine fails to capture. We find that the average TP value of extensive AR features—such as area, total unsigned magnetic flux, and total unsigned current helicity—and flux near the polarity inversion line remain constant for days before and after flares, characterizing flare-productive states for ARs. Total unsigned current helicity is reported to be one of the most significant factors for flare forecasting using machine learning (24) and is a leading contributor for the classification of flaring and nonflaring ARs as well. However, we find that the key

signature of an imminent flare is the systematic buildup of electric currents over days as measured by absolute net current helicity and the sum of net current per polarity. This storage and release of electric current at the photosphere suggest that the subsurface field associated with flaring ARs is twisted (1, 34). From case studies of individual ARs, electric current is known to accumulate before major flares (16, 17). However, in the present study such clear trends have been observed for days before and after flares and over statistics of large numbers of ARs. We show that newly emerging ARs gradually transition to flare-productive states before their first flares. The Lorentz force was hitherto known to increase significantly only minutes before flares (18). We find, most notably in the emerging ARs before the first flares, evidence of elevated Lorentz forces exerted on the photosphere by the magnetic field in the overlying corona for days before flares.

This work demonstrates the importance of testing the machine on samples from ARs that are not part of training. Such a restriction is not explicitly imposed in any prior work related to flare forecasting using ML (e.g., refs. 24, 26, and 28). Here, we show that SHARP features corresponding to extensive AR quantities (such as total unsigned flux, area, etc.) are leading contributors to the machine classification and that the average values of these SHARP features do not change appreciably over a timescale of a few days. A machine trained on observations from a set of ARs, and then tested on observations from the

same ARs (albeit for different flares), is likely to have higher *recall* because it has already added to its memory the information it saw in training, namely a similar set of SHARP features. Hence, for accurate testing of the machine, it is important that training and test data do not contain observations from the same ARs.

Class imbalance between flaring and nonflaring ARs implies that even a false-positive rate of ~ 0.1 leads to a significant number of nonflaring ARs being classified as flaring. These FP magnetic fields are from large-scale ($\sim 200 \text{ Mm}^2$) nonflaring ARs with high values of extensive AR features. Moreover, FN magnetic fields are from small-scale ARs ($\sim 100 \text{ Mm}^2$). We see that the average FN value of nonpotential energy shows a sharp increase hours before the flare (Figs. 3E and 4E), possibly caused by rapidly emerging flux (Fig. 4D). These preflare temporal patterns in small-scale flaring ARs may be accurately captured by ML algorithms trained explicitly on time series data (35). Thus, achieving reliable flare forecasting requires looking beyond extensive AR features and focusing on signatures of electric current buildup and rapidly emerging flux.

ACKNOWLEDGMENTS. D.B.D. is thankful to Andrés Muñoz-Jaramillo and Monica Bobra for insightful discussions. S.M.H. acknowledges funding from the Ramanujan fellowship; the Max-Planck partner group program; and the Center for Space Science, New York University, Abu Dhabi. Computing was performed on the SEISMO cluster at the Tata Institute of Fundamental Research.

- Cheung MCM, Isobe H (2014) Flux emergence (theory). *Living Rev Solar Phys* 11:3.
- Stein RF (2012) Solar surface magneto-convection. *Living Rev Solar Phys* 9:4.
- Leka KD, Canfield RC, McClymont AN, van Driel-Gesztelyi L (1996) Evidence for current-carrying emerging flux. *Astrophys J* 462:547.
- Shibata K, Magara T (2011) Solar flares: Magnetohydrodynamic processes. *Living Rev Solar Phys* 8:6.
- Su Y, et al. (2013) Imaging coronal magnetic-field reconnection in a solar flare. *Nat Phys* 9:489–493.
- Eastwood JP, et al. (2017) The economic impact of space weather: Where do we stand? *Risk Anal* 37:206–218.
- McIntosh PS (1990) The classification of sunspot groups. *Solar Phys* 125:251–267.
- Rust DM, et al. (1994) Preflare state. *Solar Phys* 153:1–17.
- Crown MD (2012) Validation of the NOAA space weather prediction center's solar flare forecasting look-up table and forecaster-issued probabilities. *Space Weather*, 10.1029/2011SW000760.
- Barnes G, et al. (2016) A comparison of flare forecasting methods. I. Results from the "all-clear" workshop. *Astrophys J* 829:89.
- Schrijver CJ (2009) Driving major solar flares and eruptions: A review. *Adv Space Res* 43:739–755.
- Leka KD, Barnes G (2007) Photospheric magnetic field properties of flaring versus flare-quiet active regions. iv. A statistically significant sample. *Astrophys J* 656:1173–1186.
- Wang H, Chang L (2015) Structure and evolution of magnetic fields associated with solar eruptions. *Res Astron Astrophys* 15:145–174.
- Nitta NV, Hudson HS (2001) Recurrent flare/CME events from an emerging flux region. *Geophys Res Lett* 28:3801–3804.
- Schrijver CJ (2007) A characteristic magnetic field pattern associated with all major solar flares and its use in flare forecasting. *Astrophys J* 655:L117–L120.
- Park S-H, et al. (2008) The variation of relative magnetic helicity around major flares. *Astrophys J* 686:1397–1403.
- Kontogiannis I, Georgoulis MK, Park S-H, Guerra JA (2017) Non-neutralized electric currents in solar active regions and flare productivity. *Solar Phys* 292:159.
- Sun X, Hoeksema JT, Liu Y, Kazachenko M, Chen R (2017) Investigating the magnetic imprints of major solar eruptions with SDO/HMI high-cadence vector magnetograms. *Astrophys J* 839:67.
- Fisher GH, Berdik DJ, Welsch BT, Hudson HS (2012) Global forces in eruptive solar flares: The Lorentz force acting on the solar atmosphere and the solar interior. *Solar Phys* 277:59–76.
- Hoeksema JT, et al. (2014) The helioseismic and magnetic imager (HMI) vector magnetic field pipeline: Overview and performance. *Solar Phys* 289:3483–3530.
- Scherrer PH, et al. (2012) The helioseismic and magnetic imager (HMI) investigation for the solar dynamics observatory (SDO). *Solar Phys* 275:207–227.
- Pesnell WD, Thompson BJ, Chamberlin PC (2012) The solar dynamics observatory (SDO). *Solar Phys* 275:3–15.
- Ahmed OW, et al. (2013) Solar flare prediction using advanced feature extraction, machine learning, and feature selection. *Solar Phys* 283:157–175.
- Bobra MG, Couvidat S (2015) Solar flare prediction using SDO/HMI vector magnetic field data with a machine-learning algorithm. *Astrophys J* 798:135.
- Florios K, et al. (2018) Forecasting solar flares using magnetogram-based predictors and machine learning. *Solar Phys* 293:28.
- Jonas E, Bobra M, Shankar V, Hoeksema JT, Recht B (2018) Flare prediction using photospheric and coronal image data. *Solar Phys* 293:48.
- Raboonik A, Safari H, Alipour N, Wheatland M (2017) Prediction of solar flares using unique signatures of magnetic field images. *Astrophys J* 834:11.
- Nishizuka N, et al. (2017) Solar flare prediction model with three machine-learning algorithms using ultraviolet brightening and vector magnetograms. *Astrophys J* 835:156.
- Huang X, et al. (2018) Deep learning based solar flare forecasting model. I. Results for line-of-sight magnetograms. *Astrophys J* 856:7.
- Hurlburt N, et al. (2012) Heliophysics event knowledgebase for the solar dynamics observatory (SDO) and beyond. *Solar Phys* 275:67–78.
- Bobra MG, et al. (2014) The helioseismic and magnetic imager (HMI) vector magnetic field pipeline: SHARPs – Space-weather HMI active region patches. *Solar Phys* 289:3549–3578.
- Sun X, et al. (2014) The CGEM Lorentz force data from HMI vector magnetograms. arXiv:1405.7353. Preprint, posted May 28, 2014.
- Wheatland MS, Litvinenko YE (2002) Understanding solar flare waiting-time distributions. *Solar Phys* 211:255–274.
- Longcope DW, Welsch BT (2000) A model for the emergence of a twisted magnetic flux tube. *Astrophys J* 545:1089–1100.
- Hamdi SM, Kempton D, Ma R, Boubrabhi SF, Angryk RA (2017) A time series classification-based approach for solar flare prediction. 2017 IEEE International Conference on Big Data (Big Data), eds Nie J, et al. (IEEE, Boston), pp 2543–2551.